Rare Metal Materials and Engineering
Volume 52, Issue 5, May 2023
Available online at www.rmme.ac.cn

Science Press

Cite this article as: Kong Yao, Liu Zongde, Liu Quanbing. Effect of Laser Scanning Speed on Microstructure and Corrosion Resistance of Ni-based Alloy Coatings[J]. Rare Metal Materials and Engineering, 2023, 52(05): 1624-1632.

ARTICLE

Effect of Laser Scanning Speed on Microstructure and Corrosion Resistance of Ni-based Alloy Coatings

Kong Yao, Liu Zongde, Liu Quanbing

Key Laboratory of Power Station Energy Transfer Conversion and System, Ministry of Education, North China Electric Power University, Beijing 102206, China

Abstract: Ni-based alloy (24wt% Cr, 13wt% Mo, and balanced Ni) coatings were prepared by laser cladding technique on Q235 steel. The effects of laser scanning speed (100, 200, and 300 mm/s) on microstructure and corrosion resistance of coatings were investigated. The microstructures, phase composition, element dilution rate, microhardness, and corrosion resistance of the coatings were analyzed. Results show that coatings consist of γ-Ni(Cr, Mo, Fe) and Cr0.19Fe0.7Ni0.11 solid solution. The grain size is refined, the element dilution rate is decreased, and the microhardness is enhanced with increasing the laser scanning speed. The coating prepared at scanning speed of 100 mm/s exhibits the lowest corrosion potential after immersion in 3.5wt% NaCl solution for 2 h due to its high element dilution rate. Whereas this coating shows better corrosion resistance than the other two coatings do after immersion in 3.5wt% NaCl solution for 7 d due to the good coating quality and stable passive film.

Key words: laser scanning speed; microstructure; corrosion resistance; Ni-based alloy coating

With the development of technology, many industrial applications are served under aggressive environments, such as high temperature, high pressure, and corrosive media[1]. Q235 steel has been widely used in many components due to its low cost. However, the inferior corrosion resistance of Q235 steel, particularly in Cl^--rich environment[2–3], significantly restricts its application. Therefore, it is necessary to improve the corrosion resistance of Q235 steel for stable and long-term service. Ni-based alloys, such as Hastelloy C22 alloy and Hastelloy C276 alloy, present superior corrosion resistance against pitting, crevice, and stress corrosion[4–8], which are commonly used for corrosion protection against chlorine[9–10]. However, the high cost of Ni-based alloys restricts their application. Coatings have excellent corrosion resistance performance with low cost, thereby prolonging the service life of the components[3]. Laser cladding is an advanced technique in surface protection and maintenance of components with low cost[11–15]. In addition, the coatings prepared by laser cladding are strongly metallurgical-bonded with the substrate. Thus, the good mechanical properties of the substrate material can be maintained. Other conventional techniques, such as thermal spraying and plasma transferred arc welding[16–18], can improve the surface protection but at the cost of the reduction in mechanical properties.

Nowadays, in order to improve the corrosion resistance of components, the Ni-based coatings prepared by laser cladding attract much attention. The laser cladded C22 coatings show good corrosion resistance in both static and cavitation acid solutions[19]. Wang et al[20] found that the laser cladded Ni-based alloy has enhanced mechanical and anti-corrosion properties. However, some defects, such as cracks and inclusions, can be observed under inappropriate processing, which deteriorates the microstructure and performance of coatings[21–25]. Therefore, laser cladding parameter control is of great significance in element dilution, surface quality, and corrosion resistance of coatings. The influence of process parameters of laser cladding on the microstructure and performance of coatings has been extensively researched. Ming et al[26] studied the effects of powder feeding rate on the width-to-height ratio of coating and element dilution, and found that both the width-to-height ratio and element dilution are decreased with increasing the powder feeding rate. Moosa et al[27] found the similar trend of powder dilution: the faster the laser scanning speed, the smaller the powder dilution. Li et

Received date: June 27, 2022
Corresponding author: Liu Zongde, Ph. D., Professor, Key Laboratory of Power Station Energy Transfer Conversion and System, Ministry of Education, North China Electric Power University, Beijing 102206, P. R. China, Tel: 0086-10-61772812, E-mail: lzd@ncepu.edu.cn

al[28] found that the microhardness of Ti-based coatings is firstly increased and then decreased with increasing the laser scanning speed. Jiao et al[29] found that the T15M coating prepared at laser scanning speed of 200 mm/min has small grain size with high solid solubility. Wang et al[14] revealed that the microhardness and corrosion resistance of C22 coating prepared at laser scanning speed of 12 mm/s are significantly improved, compared with those prepared at 6 mm/s. However, the influence of laser scanning speed on surface quality, element dilution rate, and corrosion resistance of Ni-based coating is rarely reported.

In this research, the Ni-based coatings were prepared by laser cladding on Q235 steel. The comprehensive effects of laser scanning speed (100, 200, and 300 mm/s) on the microstructure, surface quality, element dilution rate, and corrosion resistance of coatings were investigated.

1 Experiment

The Q235 steel with the size of 100 mm×100 mm×10 mm was used as the substrate material. Ni-based powder was used as the cladding material. The chemical composition of Ni-based powder and Q235 steel substrate is listed in Table 1. The particle diameter of Ni-based powder (Beijing General Research Institute of Mining and Metallurgy, BGRIMM, Beijing, China) was 45–109 μm. The morphology of Ni-based powder was observed by scanning electron microscope (SEM), as shown in Fig.1. Before laser cladding process, the powder was dried in the DH-101 Elector-thermostatic blast oven to ensure the fluidity. In order to remove the surface impurity, the substrate was ground and subsequently cleaned with alcohol.

The laser cladding system consisted of a fiber laser equipment (ZKZM-3000, 3 kW, Xi'an, China) as energy source, a three-axis computer-controlled workbench, a fiber laser cooling system (HL-3000-QG2/2, Wuhan, China), and a continuous coaxial powder feeding equipment. To prevent the molten oxidation in cladding process, the continuous high purity argon was used as shielding gas with flow rate of 15 L/min and as the carrier gas for powder transportation with flow rate of 5 L/min. Ni-based powder was ejected through the powder feeding nozzle and converged on the substrate surface at about 15 mm below the nozzle tip. The schematic diagram of the coaxial powder feeding nozzle is shown in Fig.2. To evaluate the comprehensive effect of laser scanning speed on the coating microstructure and properties, the speeds of 100, 200, and 300 mm/s were used. Three coatings were prepared at different laser scanning speeds. The laser cladding process parameters are listed in Table 2.

Table 1 Chemical composition of Ni-based powder and Q235 steel (wt%)

Material	Si	S	Mn	Cr	C	P	Mo	Fe	Ni
Ni-based powder	-	-	-	24	-	-	13	-	Bal.
Q235 steel	0.37	0.04	0.08	-	0.16	0.04	-	Bal.	-

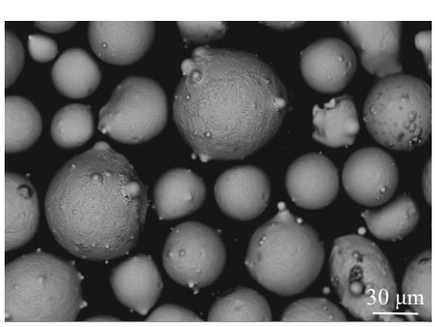

Fig.1 SEM morphology of Ni-based alloy powder

After laser cladding process, the coatings were cut into the specimens of 10 mm×10 mm×10 mm by wire-electrode cutting. The surface and cross-section of specimens were ground by SiC emery paper from 400# to 2000#, then polished by corundum powder with diameter of 3 – 5 μm, ultrasonically cleaned in the ultrasonic acetone bath for 10 min, and finally dried. The specimens for SEM observation were etched in aqua regia solution (volume ratio of $HCl:HNO_3$=3:1) for 60 s.

The surface and cross-section microstructures of coatings were observed by SEM (ZEISS EVO 18, Berlin, Germany). The element dilution of the coatings was measured by energy dispersive spectroscope (EDS, Bruker, Billerica, MA, USA). The phase composition was analyzed by X-ray diffractometer (XRD, Rigaku D/Max-2400, Tokyo, Japan). The cross-section microhardness of coatings was tested by FM-300 Vickers hardness tester at load of 500 g with the dwell time of 15 s.

The corrosion behavior of coatings was investigated by electrochemical tests. The specimens for electrochemical tests were covered by silica gel with an exposed area of 10 mm×10 mm. The tests were conducted by an electrochemical workstation (CHI760, Huachen, Shanghai, China) in 3.5wt% NaCl solution at room temperature. The conventional three-electrode system was used with a saturated calomel electrode

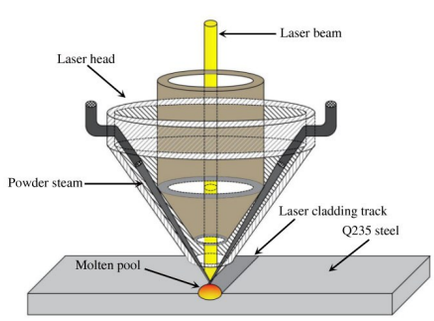

Fig.2 Schematic diagram of coaxial powder feeding nozzle

Table 2 Laser cladding process parameters

Coating	Laser power/W	Laser scanning speed/mm·s^{-1}	Overlap rate	Spot diameter/mm
A1	2400	100	0.8	2
A2	2400	200	0.8	2
A3	2400	300	0.8	2

(SCE) as the reference electrode, a platinum (Pt) as counter electrode, and the coating surface as the working electrode. Before polarization measurement, the open circuit potential (OCP) was measured for 1 h to ensure the stable potential. Potentiodynamic polarization curves were tested with scanning speed of 1 mV/s. The electrochemical impedance spectroscopy (EIS) was measured after immersion under the frequency from 100 kHz to 10 mHz for 2 h and 7 d.

2 Results and Discussion

2.1 Cross-section microstructure of coatings

Fig. 3 shows the cross-section morphologies of coatings prepared at 100, 200, and 300 mm/s. The fusion lines (red dot lines in Fig. 3) can be clearly observed between the coating and substrate. The fusion line of A1 coating shows an arc shape, whereas the other two coatings have nearly straight fusion lines. Because the input energy is different at different laser scanning speeds, it results in different molten pool depths. The A1 coating prepared at 100 mm/s has the deepest molten pool.

The surface microstructures of coatings prepared at 100, 200, and 300 mm/s are shown in Fig. 4. All coatings exhibit the similar microstructure characteristics: the coatings mainly consist of the dark dendritic grains and white interdendritic grains. The grain size is decreased with increasing the laser scanning speed. The average grain size of A3 coating is obviously smaller than that of other two coatings. The finer and more compact grains in A3 coating surface are related to the fast cooling rate at high laser scanning speed, indicating that the cooling rate plays a crucial role in the grain size control of coatings. Due to the relatively slow laser scanning speed, A1 coating has relatively coarse grains.

The cross-section microstructures of bottom, middle, and top areas of A1–A3 coatings are shown in Fig. 5. The coating microstructures are composed of bright dendrites and dark eutectics. Dendrite usually grows far away from the plane interface with stability limit and its growth orientation is along the preferred crystallographic orientation. The microstructure composition mainly depends on the temperature gradient (G) and solidification rate (R), which is usually reflected through the G/R ratio from the bonding zone to coating top. Fig. 5a–5c show that the A1 coating microstructures from top to bottom is dendrite, equiaxed dendrite, and dendrite, respectively. At A1 coating bottom, the columnar solidification without the secondary dendrite is dominant due to the larger G/R ratio at the interface between coating and substrate. The high cooling rate means the fast solidification, resulting in the fact that the secondary dendrites have insufficient time to grow. The growth direction is along the heat flow direction and perpendicular to the boundary. The cellular grains are uniformly distributed at the middle area of A1 coating. With the solidification continuously proceeding, the latent heat of crystallization is released, thereby decreasing the temperature gradient. As a result, most dendrites develop into the cellular dendrites. At A1 coating top, the heat is transferred outwards in all directions. Because of the faster cooling rate, the G/R ratio becomes smaller. The microstructure grows into fine equiaxed dendrites and a small amount of columnar crystal with disorderly growth direction exists.

At laser scanning speed of 200 mm/s, the cooling rate is

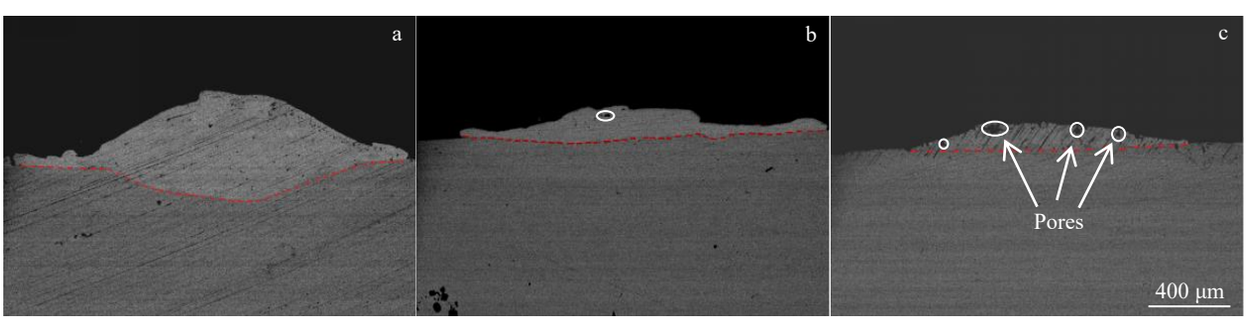

Fig.3 Cross-section morphologies of A1 (a), A2 (b), and A3 (c) coatings

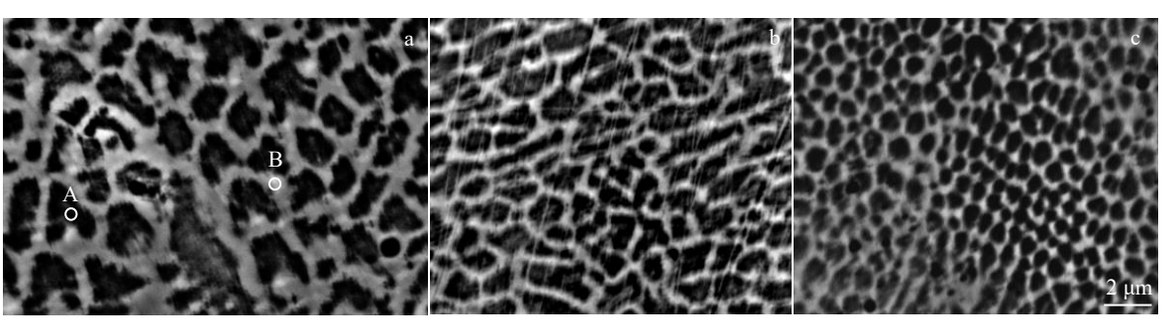

Fig.4 Surface microstructures of A1 (a), A2 (b), and A3 (c) coatings

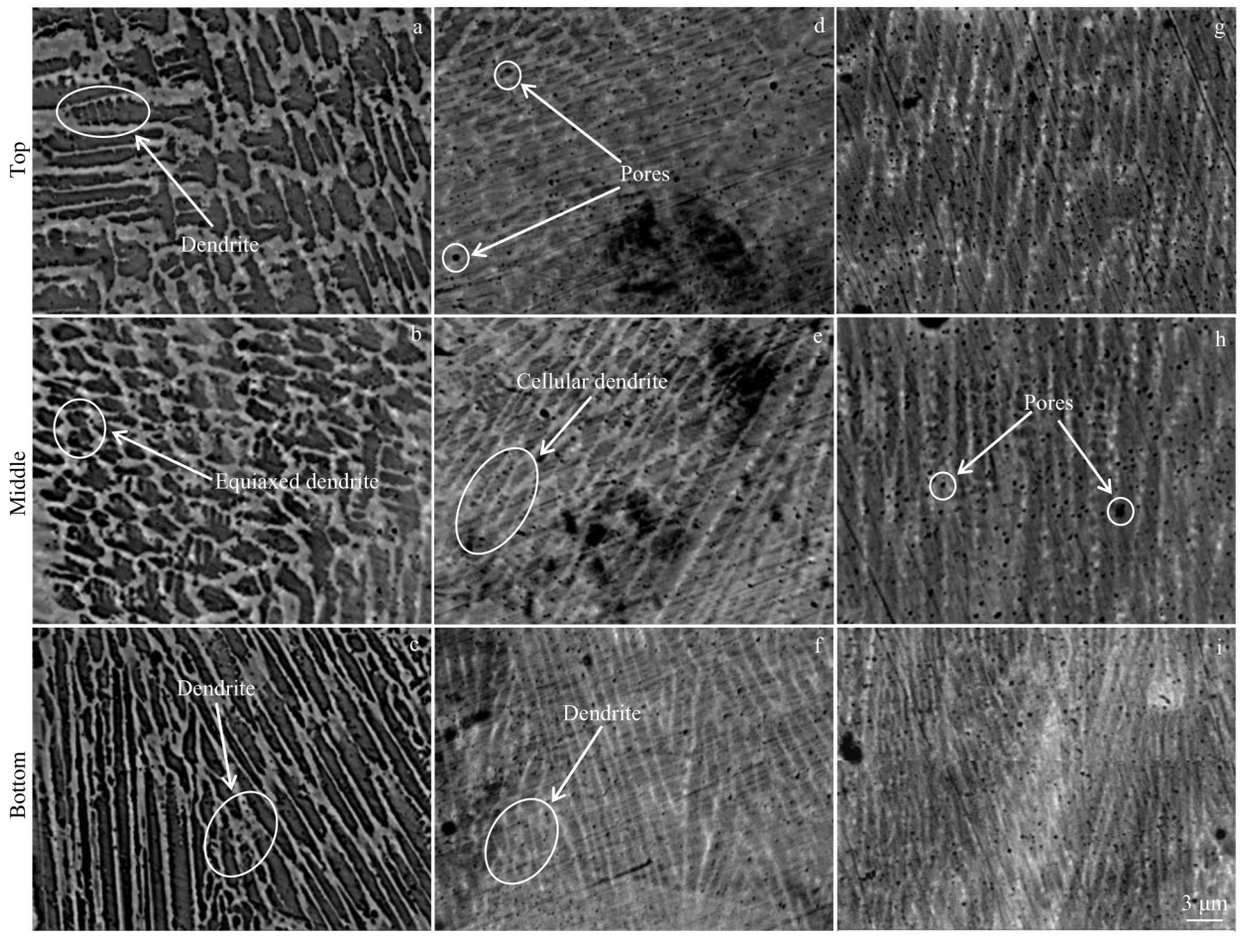

Fig.5 Cross-section microstructures of top (a, d, g), middle (b, e, h), and bottom (c, f, i) areas of A1 (a–c), A2 (d–f), and A3 (g–i) coatings

accelerated and the temperature gradient of coating becomes larger. Fig. 5d–5f show the A2 coating microstructures from top to bottom. A large number of finer and more compact dendrites can be observed at the A2 coating bottom. The A2 coating top is mainly composed of cellular dendrites. Fig. 5g–5i show the A3 coating microstructures from top to bottom. With increasing the laser scanning speed to 300 mm/s, the bottom and middle areas of A3 coating have fine dendrites, and fine cellular crystal appears nearby the coating top. This is attributed to relatively lower energy input and faster cooling rate. Compared with A1 coating, the microstructures of A2 and A3 coatings are finer with reduced primary dendrite arm spacing. However, more pores can be observed in A2 and A3 coatings, compared with those in A1 coating.

Because XRD patterns of A1–A3 coatings are similar, only XRD pattern of A1 coating is presented in Fig. 6 for discussion. The diffraction peaks are mainly related to γ-Ni solid solution with the solution of Cr, Mo, and Fe, leading to the slight shift of relevant peaks[30]. The Cr0.19Fe0.7Ni0.11 phase can also be detected. The fast cooling rate during laser cladding process leads to the formation of all structures[30]. Besides, the Cr0.19Fe0.7Ni0.11 and γ-Ni solid solution phases may exist in both the primary solidification and eutectics according to the element composition in different regions of coating by EDS analysis.

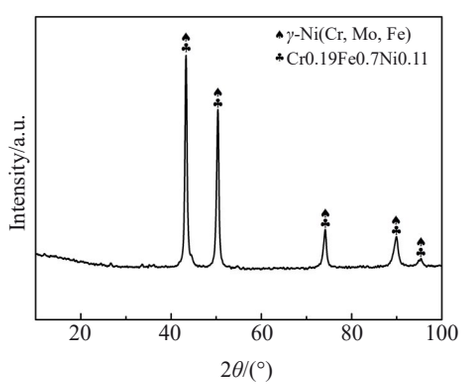

Fig.6 XRD pattern of A1 coating

The element composition of point A and point B in Fig.4a is listed in Table 3. The A1 coating is composed of the dark phase (point A) and white phase (point B). According to EDS

Table 3 EDS element composition of point A and point B in Fig.4a (wt%)

Point	Ni	Cr	Mo	Fe
A	60.17	18.95	13.22	7.66
B	53.9	21.99	18.15	5.96

analysis results, the Ni, Cr, Mo, and Fe elements can be found in both two phases. The Mo content of point B is higher than that of point A, which suggests that Mo tends to aggregate at grain boundary. Combined with XRD results, it can be inferred that the γ-Ni(Cr, Mo, Fe) solid solution and Cr0.19-Fe0.7Ni0.11 phases exist in different regions of coating.

2.2 Element diffusion of coating

The element dilution rate is evaluated through the Fe diffusion from the substrate to coating. Although the element dilution between the substrate and coating can ensure the good metallurgical bonding, the overhigh element dilution rate is not desirable in the application of laser cladded coatings. Appropriate Ni/Cr content is the fundamental mechanism for the excellent corrosion resistance of Ni-based alloys.

EDS line scanning results of Ni, Cr, and Fe element contents in the cross-section of coatings are shown in Fig. 7. The Fe content sharply decreases at the heat-affected zone in all coatings. The average Fe content of A1 coating is around 4.5wt%, whereas that of A2 and A3 coatings is obviously less than 1wt%. The increase in laser scanning speed indicates the decrease in heat input at per unit time, which efficiently reduces the Fe diffusion from substrate to the coating. The Fe content is nearly 0wt% in the top area of coatings. The Fe content in the substrate is the highest of nearly 100wt%.

According to Fig.7, Ni and Cr can hardly be detected at the heat-affected zone of all coatings. The Ni and Cr contents are stable in the coatings with only a slight increase in top area of the coatings. Besides, the Ni and Cr contents in A1 coating are lower than those in A2 and A3 coatings, which suggests that the laser scanning speed has effects on the Ni and Cr contents in the coatings. With increasing the laser scanning speed, the element dilution rate of the coatings is decreased. Thus, the Cr and Ni contents in A2 and A3 coating are close to those of raw Ni-based powder, whereas the Cr and Ni contents in A1 coating is slightly less than those of original powder. As a result, the element diffusion is effectively hindered with increasing the laser scanning speed. The fast laser scanning speed leads to insufficient energy and time for element diffusion.

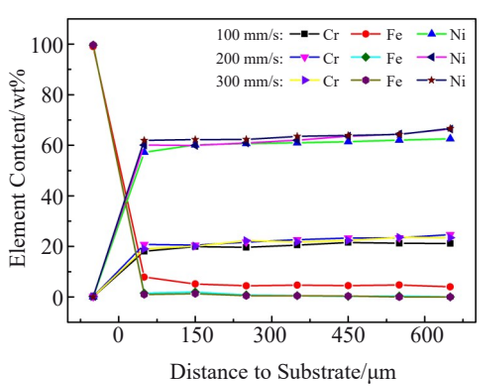

Fig.7 EDS line scanning results of element content from substrate to coating surface under different laser scanning speeds

2.3 Microhardness

The longitudinal microhardness of the cross-section of A1–A3 coatings is shown in Fig.8. The microhardness curves can be divided into three regions: coating region, heat-affected zone, and substrate region. It can be seen that the coatings have high microhardness, which is almost twice of the substrate microhardness. The microhardness fluctuates dramatically at the heat-affected zone of all coatings. According to Fig. 8, the laser scanning speed has significant effects on the microhardness of coatings. The average microhardness of A3 coating is about 3234 MPa, which is higher than that of A2 coating (3038 MPa) and A1 coating (2842 MPa). With increasing the laser scanning speed, the microhardness is increased. According to Fig.4 and Fig.5, the grain size is decreased with increasing the laser scanning speed. The average microhardness of A3 coating is higher than that of A1 coating by 15%, which results from its strong fine grain strengthening and solid solution strengthening effects. In the heat-affected zone, the Ni-based powder and substrates are mixed, which improves the microhardness of substrate area near the interface due to the solid solution strengthening. In addition, the laser scanning speed has no significant effect on the microhardness of substrate, whose microhardness is about 1568 MPa.

2.4 Electrochemical measurement

The polarization curves of A1–A3 coatings after immersion in 3.5wt% NaCl solution for 2 h and 7 d are plotted in Fig.9. The parameters of potentiodynamic polarization curves are listed in Table 4. I_{corr} represents the corrosion current density and E_{corr} represents the corrosion potential. The values of I_{corr} and E_{corr} are obtained through the Tafel extrapolation method. According to Fig. 9, the coatings have better corrosion resistance with the anodic passive behavior. The Cr_2O_3 passive film forms on the coating surface, protecting the coating from Cl^- penetration[31]. The polarization curves fluctuate a little at high anodic potentials, which may be affected by the pores in coatings. The pores can damage the density of passive film, but the passive film can heal automatically.

After immersion for 2 h, A2 coating has the most positive corrosion potential of −0.271 V and a relatively low corrosion

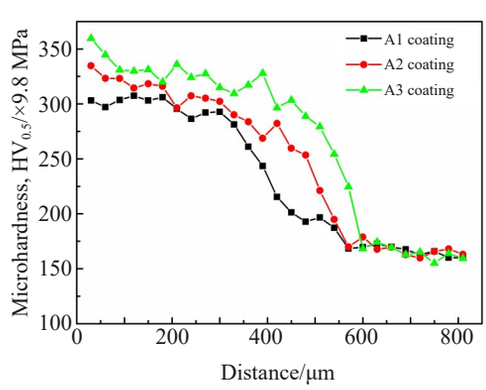

Fig.8 Microhardness of cross-section of A1–A3 coatings

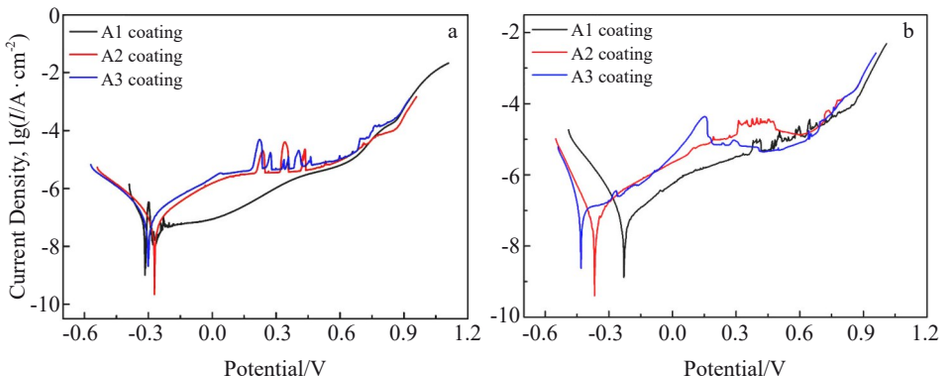

Fig.9 Polarization curves of A1–A3 coatings after immersion in 3.5wt% NaCl solution for 2 h (a) and 7 d (b)

Table 4 Electrochemical parameters of A1–A3 coatings after immersion in 3.5wt% NaCl solution for 2 h and 7 d

Coating	Immersion for 2 h		Immersion for 7 d	
	Corrosion potential, E_{corr}/V	Corrosion current density, I_{corr}/A·cm^{-2}	Corrosion potential, E_{corr}/V	Corrosion current density, I_{corr}/A·cm^{-2}
A1	−0.316	5.502×10^{-9}	−0.229	7.258×10^{-8}
A2	−0.271	9.703×10^{-8}	−0.367	6.211×10^{-8}
A3	−0.301	1.266×10^{-7}	−0.431	1.835×10^{-7}

current density of 9.703×10^{-8} A/cm^2. The A1 coating has the most negative corrosion potential of −0.316 V and the lowest corrosion current density of 5.502×10^{-9} A/cm^2, indicating that the A1 coating has higher corrosion tendency than others. The A3 coating has the maximum I_{corr} of 1.266×10^{-7} A/cm^2. Combined with Fig. 7, the lower content of Ni and Cr in A1 coating may be detrimental to the formation of passive film in the short time, compared with the case of A2 and A3 coatings. Therefore, A1 coating has weak protection effect against Cl^- corrosion. The corrosion current density of A2 and A3 coatings is much larger than that of A1 coating. More pores can be found in A2 and A3 coatings, which may accelerate the penetration of Cl^- through the coatings.

The corrosion potential of A1 coating (− 0.229 V) is increased after immersion for 7 d, compared with that after immersion for 2 h. Whereas the corrosion potential of A2 and A3 coatings is decreased with the immersion proceeding. These results suggest that the passive film on the surface of A1 coating is stable during the immersion for 7 d. However, E_{corr} of A2 and A3 coatings is decreased, compared with that after immersion for 2 h, indicating the degraded corrosion ressistance, which suggests that the coating quality rather than the Ni/Cr content plays a more important role in the density remaining for passive film during long time immersion. Pores in the surface of A2 and A3 coatings may damage the integrity of passive films, thereby decreasing the corrosion potential of A2 and A3 coatings and leading to the higher tendency for corrosion occurrence. Furthermore, it is inferred that A3 coating has the maximum I_{corr} (1.835×10^{-7} A/cm^2) due to the existence of a large number of pores.

EIS analysis provides more detailed information about the corrosion behavior of coatings after immersion in 3.5wt% NaCl solutionfor 2 h and 7 d. The Nyquist plots are shown in Fig. 10 to characterize the performance of passive films formed on the surfaces of A1 – A3 coatings. The corrosion resistance of the A1 – A3 coatings can be evaluated by the radius of fitted Nyquist plots. The larger the radius, the better the corrosion resistance[32]. According to Fig.10a, the radius of Nyquist plot of A2 coating is the largest, followed by A1 and A3 coatings. The results suggest that the passive film on the A1 coating surface is damaged after immersion in 3.5wt% NaCl solution for 2 h due to the low content of Cr and Ni elements. However, the radius of the Nyquist plot of A2 coating is sharply decreased after immersion in 3.5wt% NaCl solution for 7 d, implying that the corrosion performance of coating is deteriorated. This result is related to the pores in A2 coating, which decrease the integrity of passive film after long-term immersion in Cl^--rich environment. Besides, the radius of Nyquist plot of A1 coating is stable after immersion for 7 d, compared with that after immersion for 2 h.

Fig. 11 presents the surface morphologies of A1 – A3 coatings after immersion in 3.5wt% NaCl solution for 7 d. No obvious intergranular corrosion occurs, which is related to the existence of the passive film. However, some pit corrosion sites can be found on the surface of A2 and A3 coatings. According to Fig. 11b and 11c, the slight pit corrosion occurs around the pores. The surface of A1 coating is relatively intact without corrosion or pores. This result further confirms that the corrosion resistance of A1 coating is better than that of the other two coatings after immersion for 7 d, i. e., the better coating quality plays an important role in the formation of stable passive film, which can effectively prevent the Cl^-

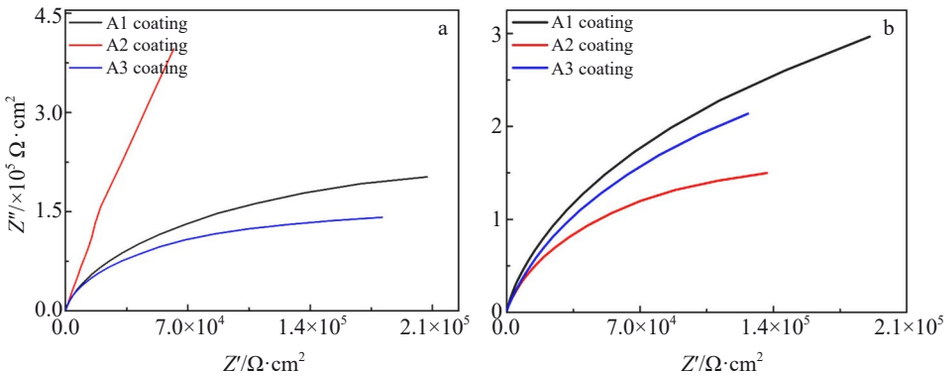

Fig.10 Nyquist plots of A1–A3 coatings after immersion in 3.5wt% NaCl solution for 2 h (a) and 7 d (b)

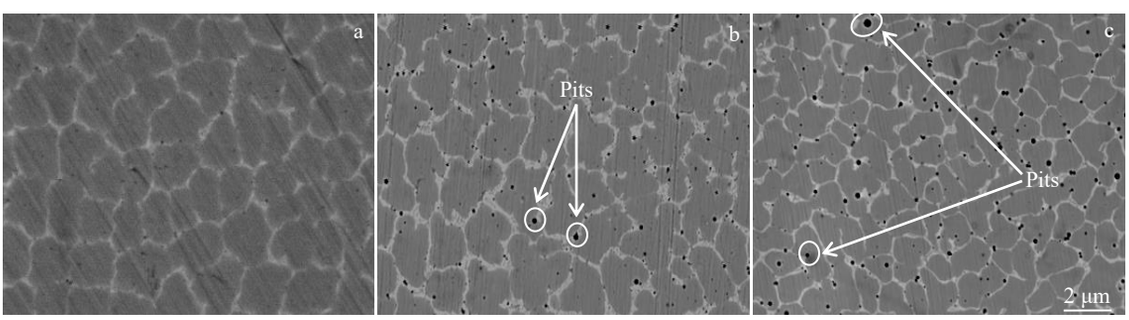

Fig.11 Surface morphologies of A1 (a), A2 (b), and A3 (c) coatings after immersion in 3.5wt% NaCl solution for 7 d

penetration.

The corrosion behavior of Ni-based coatings consists of anodic oxidation process, as well as the formation and dissolution of passivation film[19–20]. The anodic polarization process is as follows:

$$Ni+H_2O=Ni(OH)_{ad}+H^++e^- \quad (1)$$

$$Ni(OH)_{ad}=Ni(OH)^++e^- \quad (2)$$

$$Ni(OH)^++H^+=Ni^{2+}+H_2O \quad (3)$$

$$Cr+H_2O=Cr(OH)_{ad}+H^++e^- \quad (4)$$

$$Cr(OH)_{ad}=Cr(OH)^++2e^- \quad (5)$$

$$Cr(OH)^{2+}+H^+=Cr^{3+}+H_2O \quad (6)$$

The formation rate of passivation film reaches a steady state with increasing the electrodynamic potential. The passivation range can be observed on the polarization curves, as shown in Fig.9. The passivation reactions occur on the coating surface, as follows:

$$Ni(OH)_{ad}+H_2O=[Ni(OH)_2]_{ad}+H^++e^- \quad (7)$$

$$[Ni(OH)_2]=NiO+H_2O \quad (8)$$

$$Cr(OH)_{ad}+2H_2O=[Cr(OH)_3]_{ad}+2H^++2e^- \quad (9)$$

$$2[Cr(OH)_3]=Cr_2O_3+3H_2O \quad (10)$$

The anode current increases gradually when the potential reaches over passivation potential, causing pitting corrosion at the weak area of passivation film[33]. Dissolution of passivation film in Cl^- containing medium is shown in Eq. (11 – 12) as follows:

$$NiO+2Cl^-+H_2O=NiCl_2+2OH^- \quad (11)$$

$$Cr_2O_3+6Cl^-+3H_2O=2CrCl_3+6OH^- \quad (12)$$

Fig.12 shows the schematic diagrams of corrosion behavior of coatings after immersion in 3.5wt% NaCl solution for 2 h and 7 d. Due to the high element dilution rate of A1 coating, the formation process of passivation film may be slower than

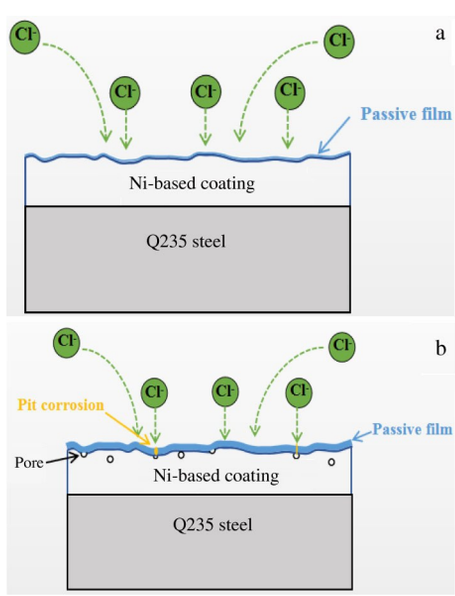

Fig.12 Schematic diagrams of corrosion behavior of coatings after immersion in 3.5wt% NaCl solution for 2 h (a) and 7 d (b)

that of A2 and A3 coatings. Meanwhile, the high Fe content causes a high tendency to react with Cl^-. Therefore, A1 coating exhibits inferior electrochemical performance after immersion in Cl^--rich environment for 2 h. With the immersion proceeding, the passivation reaction is completed and the passivation film is thickened. Cl^- migrates towards the coating surface and gradually penetrates the coatings. The integrity of passivation film of A2 and A3 coatings is damaged to some extent by pores, thereby causing localized corrosion. The initial pores of coatings also provide the paths for Cl^- penetration. Thus, A1 coating displays the optimal corrosion resistance due to its better coating quality without obvious pores, which indicates that Cl^- penetration is hindered by the dense and stable passive film during immersion in 3.5wt% NaCl solution.

3 Conclusions

1) The Ni-based alloy coatings and Q235 substrate have good metallurgical bonding. The laser cladded coatings mainly contain γ-Ni(Cr, Mo, Fe) and Cr0.19Fe0.7Ni0.11 solid solution phases. The dendrite, cellular grain, and equiaxed dendrite exist in the coatings. With increasing the laser scanning speed, the grains become finer and more compact, but the number of pores is also increased.

2) With increasing the laser scanning speed, the coatings have slower element dilution rate and higher microhardness. The coating prepared at laser scanning speed of 100 mm/s has the fastest element dilution rate with low Cr and Ni contents and high Fe content.

3) The coating prepared at laser scanning speed of 100 mm/s shows better corrosion resistance with high corrosion potential and low corrosion current density due to the good surface quality and stable passive film during the immersion in 3.5wt% NaCl solution for 7 d.

References

1 Dehnavi F, Eslami A, Ashrafizadeh F. *Engineering Failure Analysis*[J], 2017, 80: 368

2 Balasubramanian V, Lakshminarayanan A K, Varahamoorthy R *et al*. *Journal of Iron and Steel Research International*[J], 2009, 16(1): 44

3 da Luz F S, Pinheiro W A, Monteiro S N *et al*. *Journal of Materials Research and Technology*[J], 2020, 9(1): 636

4 Agarwal D C, Herda W R. *Materials Corrosion*[J], 1997, 48(8): 542

5 Pardo A, Merino M C, Coy A E *et al*. *Corrosion Science*[J], 2008, 50(6): 1796

6 He X, Dunn D S. *Corrosion*[J], 2007, 63(2): 145

7 Jakupi P, Wang F, Noël J J *et al*. *Corrosion Science*[J], 2011, 53(5): 1670

8 Chiang K T, Dunn D S, Cragnolino G A. *Corrosion*[J], 2007, 63(10): 940

9 Crook P. *Corrosion*[J], 2005, 56(9): 606

10 Rebak R B, Crook P. *ASME Pressure Vessels and Piping Conference*[C]. San Diego: AMSE, 2004, 46 784: 131

11 Bourahima F, Helbert A L, Rege M *et al*. *Journal of Alloys and Compounds*[J], 2018, 771: 1018

12 Xiang K, Chen L Y, Chai L *et al*. *Applied Surface Science*[J], 2020, 517: 146 214

13 Liu S, Farahmand P, Kovacevic R. *Optics & Laser Technology*[J] 2014, 64: 363

14 Wang Q Y, Zhang Y F, Bai S L *et al*. *Journal of Alloys and Compounds*[J], 2013, 553: 253

15 Fei W, Yu H J, Chen C Z *et al*. *Journal of Alloys and Compounds*[J], 2017, 692: 989

16 Khanna A S, Kumari S, Kanungo S *et al*. *International Journal of Refractory Metals and Hard Materials*[J], 2008, 27(2): 485

17 Sudha C, Shankar P, Subba R V *et al*. *Surface & Coatings Technology*[J], 2008, 202(10): 2103

18 Zhao J, Gao Q W, Wang H Q *et al*. *Journal of Alloys and Compounds*[J], 2019, 785: 846

19 Wang Q Y, Bai S L, Liu Z D. *Transactions of Nonferrous Metals Society of China*[J], 2014, 24(5): 1610

20 Wang Q Y, Bai S L, Zhang Y F *et al*. *Applied Surface Science*[J], 2014, 308: 285

21 Hidouci A, Pelletier J M, Ducoin F *et al*. *Surface & Coatings Technology*[J], 2000, 123(1): 17

22 Xu G J, Kutsuna M, Liu Z J *et al*. *Materials Science and Engineering A*[J], 2006, 417(1–2): 63

23 Wang K L, Zhang Q B, Sun M L *et al*. *Journal of Materials Processing Technology*[J], 2003, 139(1–3): 448

24 Huang F X, Jiang Z H, Liu X M *et al*. *Journal of Materials Processing Technology*[J], 2009, 209(11): 4970

25 Werner H. *Journal of Solid State Electrochemistry*[J], 2006, 10: 753

26 Ming Q, Lim L C, Chen Z D. *Surface & Coatings Technology*[J], 1998, 106(2–3): 174

27 Moosa A A, Kadhim M J, Subhi A D. *Modern Applied Science* [J], 2011, 5(1): 50

28 Li Y X, Su K Q, Bai P K *et al*. *Materials Characterization*[J], 2019, 159: 110 023

29 Jiao X Y, Wang J, Wang C M *et al*. *Optics and Lasers in Engineering*[J], 2018, 110: 163

30 Dinda G P, Dasgupta A K, Mazumder J. *Materials Science and Engineering A*[J], 2009, 509(1–2): 98

31 Wang Q Y, Pei R, Liu S *et al*. *Surface & Coatings Technology*[J], 2020, 402: 126 310

32 Jiang Y Q, Li J, Juan Y F *et al*. *Journal of Alloys and Compounds*[J], 2019, 775: 1

33 Kong Y, Liu Z D, Li B. *Rare Metal Materials and Engineering*[J], 2021, 50(8): 2694

激光扫描速度对镍基合金熔覆层显微结构和耐腐蚀性能的影响

孔　耀，刘宗德，刘泉兵

(华北电力大学 电站能量传递转化与系统教育部重点实验室，北京 102206)

摘　要：采用激光熔覆技术在Q235钢表面制备了镍基合金（含质量分数24%Cr、13%Mo）熔覆层，研究了激光扫描速度（100、200和300 mm/s）对熔覆层显微结构和耐腐蚀性能的影响，分析了熔覆层的显微组织、相组成、元素稀释率、显微硬度和耐腐蚀性能。结果表明，熔覆层由γ-Ni(C, Mo, Fe)和Cr0.19Fe0.7Ni0.11固溶体组成。随着激光扫描速度的提高，熔覆层晶粒细化，元素稀释率降低，显微硬度提高。由于元素稀释率较高，在扫描速度100 mm/s制备的熔覆层在3.5%（质量分数）NaCl溶液中浸泡2 h后的腐蚀电位最低。但由于熔覆层质量好，表面钝化膜稳定，在3.5% NaCl溶液中浸泡7 d后，其耐腐蚀性能仍优于其他2种涂层。

关键词：激光扫描速度；显微结构；耐腐蚀性能；镍基合金熔覆层

作者简介：孔　耀，男，1994年生，博士，电站能量传递转化与系统教育部重点实验室，北京 102206，E-mail：ky@ncepu.edu.cn